A new reduced order model to represent the creep induced fuel assembly bow in PWR cores

Bertrand Leturcq, Patrick Le Tallec, Serge Pascal, Olivier Fandeur, Nicolas Lamorte

To cite this version:

Bertrand Leturcq, Patrick Le Tallec, Serge Pascal, Olivier Fandeur, Nicolas Lamorte. A new reduced order model to represent the creep induced fuel assembly bow in PWR cores. Nuclear Engineering and Design, 2022, 394, pp.111828. 10.1016/j.nucengdes.2022.111828 . cea-04149355

HAL Id: cea-04149355
https://cea.hal.science/cea-04149355v1
Submitted on 4 Jul 2023

A new reduced order model to represent the creep induced fuel assembly bow in PWR cores

Bertrand Leturcq[a,b], Patrick Le Tallec[a], Serge Pascal[b], Olivier Fandeur[b], Nicolas Lamorte[c]

[a] LMS, École Polytechnique, CNRS, Institut Polytechnique de Paris, Palaiseau 91128, France
[b] Université Paris-Saclay, CEA, Service d'études mécaniques et thermiques, 91191 Gif-sur-Yvette, France
[c] Framatome, 2 rue du Professeur Jean-Bernard 69007 Lyon, France

Abstract

Progressive deformation of nuclear fuel assemblies that occurs during a succession of irradiation cycles within PWR is at the core of numerous interactions. Progresses in the study of this phenomenon resulted from more and more complex models. To date, in the more advanced models, a mechanical model is combined to a hydraulic model of the core to address the fluid-structure interaction. A complete mechanical model of the core is generally built with a simplified finite element representation of each assembly using beam or simpler elements. The simplifying approach is required due to the high complexity of the multi-body multi-physics calculations. In order to improve the representativeness of the core model without penalizing the computational cost of the coupled simulations, a new method of model order reduction is proposed. It is specially adapted to this context and borrows the concepts of NTFA non-linear homogenization. The theoretical foundations and the application to a slender structure are presented. First, the method is validated on a simple case with spatially homogeneous characteristics. Finally, the case of the creep response of a fuel assembly under realistic heterogeneous loads is demonstrated.

Highlights

- The fuel assembly bow is calculated rapidly with a physics-based reduced model
- This new *a posteriori* model reduction is inspired from non-linear homogenization NTFA
- It takes into consideration the creep heterogeneity and its variation in time
- The aim is to replace advantageously simplified beam models in FSI coupled core simulation

Keywords

PWR assembly bow, model reduction, NTFA, creep

1. Introduction

Industrial context

The fuel assemblies (FA), initially straight, deform within the core of a pressurized water nuclear reactor (PWR), see Fig. 1. A strong curvature of the guide thimbles can lead to an important friction when the control bars fall. As a result, the travel time of the bars may be increased and no longer acceptable from a safety point of view. Over time, several design improvements were performed, with positive effects on rod insertion and operation of the plant. In this regard, (Gabrielsson et al., 2018) noticed that these modifications led to a change in the shape of assembly bow, from a mainly S-shape to a C-shape, with consequences on the radial neutron flux distribution (Saeed et al., 2016). This phenomenon is studied on different axes, like neutronics, FA bow (De Lambert et al., 2019) or moderator temperature during power ramp-up strategy (Gabrielsson et al., 2018).

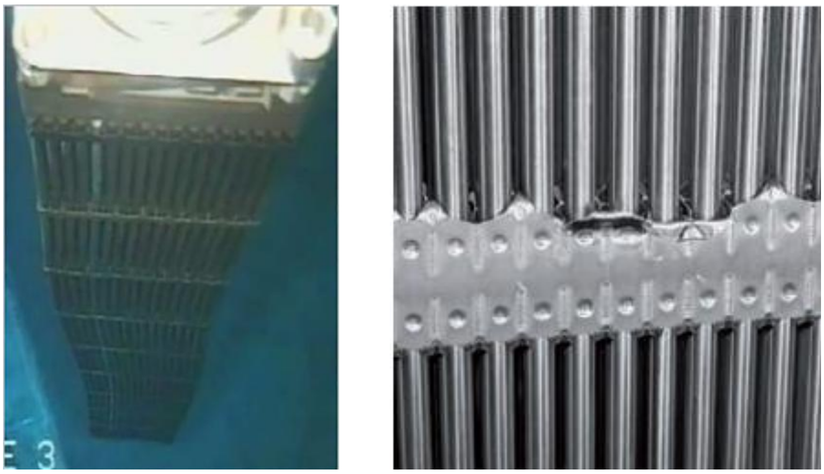

Fig. 1. View of a bowed PWR fuel assembly(Fernandes, 2010), grid damaged during handling operations (IAEA, 2010).

The quasistatic deformation of the FA increases during the several irradiation cycles of its stay in the reactor core due to the complex interaction of a number of phenomena. The main cause of the assembly bow are the lateral forces, both the contact forces with the four neighbors and the hydraulic forces. The lateral hydraulic forces vary with the position in the core and during the irradiation time (Wanninger, 2018). They are coupled to the FA bow pattern in the core, the reciprocal fluid structure interaction phenomenon being now widely studied (Horváth and Dressel, 2013; Wanninger et al., 2018). The vertical component of the hydraulic force can reach levels capable of lifting the FA if it were not maintained axially. Some studies point that the flow is also influenced by the upstream (Fournier et al., 2007) and downstream boundary conditions (Sheng and Seidl, 2015). Additionally, due to the slender geometry of the FA, an aggravating factor is the axial compression maintained by the holdown spring. Intricate internal mechanisms lead to the FA deformations under such loading conditions. The most important contributor is the irradiation creep and growth (Scholz and Matera, 2000) of zirconium alloys (Fidleris, 1988; Gharbi, 2015; Gilbon et al., 2000). Its rate is almost linear with both stress and fast neutron flux and depends on temperature (Kecek et al., 2016). Another significant phenomenon is the evolution of the interaction between the fuel rods and the supporting grids. The trapped efforts due to friction contribute to the irreversible macroscopic deformation of the FA. These effects decrease with time because of the progressive relaxation of support springs. To a lesser extent, the fast decrease of neutron flux in the peripheral positions of the core also plays a role. It tends to curve the FA towards the center of the core because the inward fuel rods grow axially faster. Consequently to capture the complexity of the FA response in PWR conditions at the scale of the entire core, it is necessary to encompass a wide range of phenomenons and, at the same time restrict the total number of degrees of freedom of the core model to keep the computational cost within a feasible range. The main objective of the core model is to be both accurate and computationally economic.

The first core studies consisted of simplified FA models arranged in two dimensional rows to limit the model size. The FA simplified model represents one or more guide thimbles connected to one or more rods at every grid levels (Jeon, 2009). They rely on beam or pipe elements for the structures and on discrete elements to represent the connections, including the multiple contacts. These relatively economical mechanical models dedicated to quasi-static evolution (Horváth and Dressel, 2013; Lamorte et al., 2021; Wanninger et al., 2018) and those more oriented for dynamic simulation (Elbanhawy et al., 2021; Hassan and Rogers, 2005; Ricciardi, 2017) now make it possible to perform calculations coupling hydraulics and mechanics. The main phenomena involved in the mechanical deformation of assemblies are often well represented. However, by construction, these models contain simplifying assumptions that alter the accuracy of the simulation. For example, the grids are non-deformable, the lateral gradient of neutron flux is omitted and, above all, the curvatures, elongations, and slippages of the rods in grids are homogenized for a large number of rods. Moreover, it remains impossible to validate experimentally these models at the scale of one FA subjected to irradiation. The correlations at the full core scale seem to give good qualitative results but are not completely predictive on a series of cycles (Lascar C., 2015; Wanninger et al., 2018, 2016).

The focus of this paper is to obtain through adequate model reduction techniques a prediction of better quality compared to the one accessible with the FA simplified finite element models, in particular with regard to the spatial distribution of non-linear quantities. At the same time, this enhancement should not increase the computing time. This paper restricts to the model reduction of a single FA subjected to heterogeneous creep. The other influent phenomena, such as contact and friction are not presented here.

A reduced order model (ROM) always relies on a detailed numerical model. This one needs to represent accurately the thermomechanical behavior of a FA under the wide range of loads representative of in-core operating conditions. This detailed model corresponds to a quasi-static irradiation creep problem using up to millions degrees of freedom, to describe the components and their structural details (rods, grids, nozzles, grid springs, dimples). It is also important to notice that the creep is proportional to irradiation, which may be heterogeneous in a FA, especially one at the periphery of the core. The irreversible FA bow is associated with rods sliding into grids and with creep strains, which typically develop over a period of one year. That is why other phenomena, like small vibrations, are neglected since they are not supposed to influence significantly the irreversible bow. Operating experience suggests that a limited number of shape modes may be sufficient to represent the macroscopic deformation of a FA (Andersson et al., 2005), (Gabrielsson et al., 2018). Therefore, model reduction techniques using modal representations seem to be the best candidate to approach this problem.

Model reduction

There are three main classes of model reduction techniques, namely Proper Orthogonal Decomposition (POD), Proper Generalized Decomposition (PGD) and hyper-reduction (HR).

The proper orthogonal decomposition is widely used in a number of applications. It is also known as Karhunen-Loeve decomposition (Karhunen, 1946), or principal components analysis. It is an efficient data analysis technique that approximates a high-dimensional system by a much lower-dimensional one. Essentially, this method is a linear procedure, which consists in looking for the eigenvectors of a spatial or time (Lumley, 1967) correlation operator. It is represented by definition of the most probable realizations. It is an *a posteriori* method, since a set of data coming from numerical simulations or experiments, called the snapshots, must be available before producing the eigenvectors and eigenvalues. In details, the method constructs the space modes $\boldsymbol{U}_j^{POD}(x)$ that give the optimal projection of all the snapshots $\boldsymbol{U}^{data}(x,t)$ in the sense of the least square, modes which turn to be the eigenvectors of the snapshots correlation matrix. Such a POD basis (1) can be used in a Galerkin POD projection to reduce the size of any linear or linearized problem. It primarily targets linear problems, with an excellent speed-up. However, in the creep problem, a linearization of the complete model at each time step would be much too expensive.

PGD stands for Proper Generalised Decomposition (Ladeveze, 1985). It is a method of construction of an orthonormal or non-orthonormal basis for the decomposition of a solution in separate space-time or space-time-parameter form. PGD is a recent method that has been used in many disciplines: for homogenization problems (Metoui et al., 2014), for structural computations with viscoelastic behavior (Hammoud et al., 2011), in fluid mechanics (Dumon et al., 2011), and even for solving the Schrödinger equation (Ammar and Chinesta, 2008). It is *a priori* method since the reduced basis is built progressively during the computation and not *a posteriori* as in the POD, where a set of results are already available. This progressive construction of the reduced basis means that one will use the initial high-dimensional model each time it will be necessary to enrich the basis, which is a guarantee of the quality of the solution as much as a price to pay to obtain it. PGD is naturally adapted to treat a creep problem. However, it is significantly more complex to implement than Galerkin POD. Finally, there is a major doubt as to its ability to achieve a computation time of the reduced model in accordance with our objective of less than one minute.

Hyper reduction is used in the APHR (*a priori* hyper-reduction) method. It is an incremental two-level adaptive basis reduction method developed by (Ryckelynck, 2009). A first reduction, called APR, concerns the global linear problem in space. It uses the snapshot POD principle several times during the computation in order to enrich the basis during the evolution. This enrichment takes place when it is required by an error indicator and calls for a complete resolution on the full scale model. The second reduction is performed for the integration of the local nonlinear behavior by means of the selection and use of a reduced number of integration points of the initial model, chosen with the discrete empirical interpolation method (DEIM) (Barrault et al., 2004). The hyper-reduction seems the best candidate at first sight, thanks to its double reduction of the balance and the number of integration points to be treated. Nevertheless, the announced time savings of the APHR, between 40% and 90%, are very far from our objective. (Hernández et al., 2017) recently proposed a new integration method limiting the size of the reduced integration domain. When used in *a posteriori* hyper-reduction, they obtain a much better speed-up, superior to 100. Unfortunately, in the near future, the authors intend to add contact and friction between rods and grids in the reduced model and, although (Fauque et al., 2018) have shown the feasibility to use hyper-reduction with contact, they obtained a speed-up far behind our present objective.

In the present model order reduction framework, our objective of being able to carry out numerous simulations of the core deformations in a very short time leads us towards *a posteriori* model reduction methods, where modal basis are fixed. The second observation is that an order reduction of the spatial problem is more advisable than a reduction of the temporal problem, because the number of degrees of freedom of the problem largely exceeds its temporal discretization. Time compression is unnecessary. The third point is again relative to the speed-up. In the *a posteriori* hyper-reduction, a significant part of the computing time is related to the number of integration points in the reduced integration domain. Reducing their number even more would be beneficial to the speed-up.

These three observations led us to define a new type of reduced order model by adapting a non-linear homogenization method to the case of a slender structure. This method is called the NTFA, for Nonlinear Transformation Field Analysis (Michel and Suquet, 2003). The NTFA is a scaling up method that uses two levels of reduction, with only one basis of tensor functions to represent the non-linear transformations. The first level considers the localization of the mean strain imposed by the upper scale and the second one permits to integrate the non-linear behavior directly as if there were only one integration point. The speed-up is therefore excellent.

In order to obtain the speed-up of the NTFA, the idea is to adapt this homogenization method to a slender structure instead of a representative volume element (RVE). In this regard, the principles of the NTFA will first be recalled in paragraph 2, before explaining its adaptation to the reduction of a slender structure model in section 2. Section 3 applies the proposed technique to a simple structure with nonlinear creep while section 4 treats the case of a creep of a PWR FA in heterogeneous conditions.

2. A new model order reduction for structures subjected to creep

2.1 The NTFA homogenization method

In the field of homogenization of nonlinear composite materials, the mean field approaches prove to be usually insufficient since they fail to consider the intraphase heterogeneity of the mechanical fields. Considering the almost infinite number of variables which describe the state of a representative volume element, (Dvorak, 1992) proposed to separate each phase in a limited number of subvolumes affected with a homogeneous plastic strain. Each subvolume obeys the phase constitutive relation. The quality of this piece-wise uniform approximation of the internal variables fields is controlled by choosing the number of subdomains. He also introduced the influence tensors, characterizing the stress perturbation induced in every subdomain by a unit stress-free transformation in a given subdomain. He named this method the Transformation Field Analysis (TFA). It permits to solve numerically a macroscopic constitutive relation with a number of averaged internal variables proportional to the number of subdomains. (Fish and Shek, 1999), (Chaboche et al., 2001) then extended the TFA use to more complex behaviors including damage mechanics. This approach effectively accounts for the nonlinear mechanical behavior of the RVE. However, the convergence of the method with the number of subdomains to the actual behavior of the medium is sometimes slow due to the function space used and may tend to an over-stiffening of the effective response of the volume element. (Michel and Suquet, 2003) have improved the TFA method, first by using a finite set of higher order, non-uniform function basis, hence the name of their method: Non-uniform Transformation Field Analysis (NTFA). Hereafter are presented the main elements of this method.

Let us consider a heterogeneous medium constituted of N phases with a linear or nonlinear behavior. The first operation is to define a representative volume element of the medium (RVE), statistically representative of the proportions and distributions of the different phases, in order to study the effective behavior of the composite medium. The second operation is to specify the constitutive laws of the different phases. The NTFA authors worked in the framework of standard generalized materials which covers a large variety of material responses. For example, (Roussette et al., 2009) explored the spherical as well as the deviatoric creep occurring in nuclear fuel, before (Largenton et al., 2013) add the hydrostatic swelling induced by an intense neutron flux. More recently (Michel and Suquet, 2016) also applied the NTFA to complex polycristalline materials such as ice.

For the sake of simplicity, let us consider a dissipative material, characterized by a free energy potential w and a force potential ψ, involving a fourth order elasticity tensor $\mathbb{L}$. The creep rate tensor $\dot{\boldsymbol{\varepsilon}}^{in}$ is deduced from ψ as follows, with σ_{eq}, the Von Mises equivalent stress, and $\boldsymbol{\sigma}'$, the stress deviator. The notation : in the formulas is for the double contraction of the tensors.

$$\begin{cases} \boldsymbol{\sigma} = \dfrac{\partial w}{\partial \boldsymbol{\varepsilon}} = \mathbb{L}:(\boldsymbol{\varepsilon} - \boldsymbol{\varepsilon}^{in}) \\ \dot{\boldsymbol{\varepsilon}}^{in} = \dfrac{\partial \psi}{\partial \boldsymbol{\sigma}} = \dfrac{3}{2}\dfrac{\partial \psi}{\partial \sigma_{eq}}\dfrac{\boldsymbol{\sigma}'}{\sigma_{eq}} \end{cases} \quad (1)$$

An orthonormal basis of M functions $\boldsymbol{\mu}_k$ $(1 \leq k \leq M)$, called modes is introduced typically using a proper orthogonal strategy (POD) on a given set of snapshots. Each mode is a symmetric field of tensor of order 2 defined in a single phase of the composite. The set of modes covers all non-linear phases. The projection ε_k of any second order tensor field $\boldsymbol{\varepsilon}$ onto a mode k is defined by:

$$\varepsilon_k = \frac{1}{V}\iiint \boldsymbol{\varepsilon}:\boldsymbol{\mu}_k \, dV \quad (2)$$

The basis of functions $\boldsymbol{\mu}_k$ is orthonormal and normalized such that each mode is homogeneous to a plastic strain:

$$\begin{cases} \iiint \boldsymbol{\mu}_p : \boldsymbol{\mu}_q \, dV = 0 \; \forall p \neq q \\ \dfrac{1}{V} \iiint \boldsymbol{\mu}_p : \boldsymbol{\mu}_p \, dV = \sqrt{\dfrac{3}{2}} \end{cases} \qquad (3)$$

where δ_{pq} is the Kronecker symbol. Moreover, the support of each mode is entirely contained in a single material phase. In our case, the modes will also be purely deviatoric.

The first major approximation of the NTFA method is to assume that the inelastic tensor ε^{in} can be developed on this modal basis:

$$\varepsilon^{in} = \sum_{p=1}^{M} \boldsymbol{\mu}_p \varepsilon_p^{in}$$

The local solution of the equilibrium problem inside a Representative Volume Element with constitutive law (9) and imposed averaged deformation $\overline{\boldsymbol{E}}$ is then given explicitly by:

$$\boldsymbol{\sigma} = \mathbb{L} : \boldsymbol{A} : \overline{\boldsymbol{E}} + \sum_{p=1}^{M} \mathbb{L} : (\boldsymbol{D}_{p-} \boldsymbol{\mu}_p) \varepsilon_p^{in}$$

where the localization tensor field $\boldsymbol{A}$ and influence tensor $\boldsymbol{D}_p$ can be computed a priori by solving the same equilibrium problem respectively with a unit imposed average deformation or inelastic component. The projection of the local stress field onto a given mode is then given by:

$$\sigma_k = \left[\frac{1}{V} \iiint \mathbb{L} : \mathbb{A} : \boldsymbol{\mu}_k dV \right] : \overline{\boldsymbol{E}} + \sum_{p=1}^{M} \left[\frac{1}{V} \iiint \boldsymbol{\mu}_k : \mathbb{L} : \left(\mathbb{D} * \boldsymbol{\mu}_p - \boldsymbol{\mu}_p \right) dV \right] \varepsilon_p^{in} \qquad (4)$$

The terms in square brackets can be calculated a priori by performing a single elastic calculation over the RVE for each mode k. $\overline{\boldsymbol{E}}$ is supposed to be known but the inelastic components ε_p^{in}, which are subject to time evolution are not determined.

The standard homogenization method requires updating the inelastic components ε_p^{in} in each phase to compute the local stress. In the so-called "hybrid" method, it is possible to perform an exact integration of the constitutive relations at any point of the RVE but at the expense of simulation time. In order to drastically reduce the cost of the calculations, the evolution problem of the internal variables needs to be solved directly in the basis of modes $\boldsymbol{\mu}_k$. (Rice, 1970) and (Michel and Suquet, 2004) have shown that, when the constitutive laws derive as above from two potentials, their structure can be transposed in the reduced basis. More precisely, the original flow rules projected on the modal basis is given by:

$$\dot{\varepsilon}_k^{in} = \frac{1}{V} \iiint \dot{\boldsymbol{\varepsilon}}^{in} : \boldsymbol{\mu}_k dV = \frac{1}{V} \iiint \frac{3}{2} \frac{\partial \psi}{\partial \sigma_{eq}} \frac{\boldsymbol{\sigma}' : \boldsymbol{\mu}_k}{\sigma_{eq}} dV \qquad (5)$$

To obtain a relationship between the reduced internal variables $\dot{\varepsilon}_k^{in}$ and the σ_k, it is necessary to make an approximation of σ_{eq} in order to simplify (5). A possible approximation is given by (Michel and Suquet, 2003) who estimate a global reduced stress s_r for the phase r by the Euclidian norm of the $M(r)$ modal stresses

$$s_r = \sqrt{\sum_{p=1}^{M(r)} \sigma_p^2} \qquad (6)$$

By replacing (6)into (5) they finally obtain the approximate coupled reduced evolution law that enables to update the inelastic state variables ε_k^{in} by:

$$\dot{\varepsilon}_k^{in} = \frac{3}{2} \frac{\partial \psi(s_r)}{\partial \sigma_{eq}} \frac{\sigma_k}{s_r} \qquad (7)$$

This strategy has been validated by (Michel, Suquet, 2004) looking at the load-displacement curves of a four-point bending case simulated on half a composite beam comparing a reference model to an homogenized result based on NTFA.

2.2 Adaptation of the NTFA method to a slender structure

Following the NTFA approach, the main idea is to consider that a fuel assembly (FA) constitutes a representative volume element (RVE) of the core. The main difficulty comes from the fact that the envelope of this RVE has a slender shape whose average deformation cannot be reduced to a classical symmetric deformation tensor $\overline{\boldsymbol{E}}$. Indeed, the FA is likely to deform according to a large number of shapes including elongations, C-curvature, S-curvature, W-curvature and this, in different directions. The main adaptation with respect to the NTFA is therefore to define the average deformed shape of this structural RVE using a basis of macroscopic displacement modes.

Obviously, there is a compromise to find on the number of these macoscopic modes, willingly minimal to lower the computational cost of the model, and high enough to represent the FA bows with sufficient precision.

Once this point of determining the macroscopic displacement modes is acquired, one must then construct the orthogonal basis of the inelastic strains within the RVE. By considering each of these internal strain mode or macroscopic displacement modes as individual loadings, one can reconstruct the local stress field everywhere. First, this allows to check the static equilibrium on the displacement modes, then to derive the thermodynamic forces that guide the evolution of the inelastic deformations, namely the amplitude of the creep modes in our case. For this, the projection of the local evolution law leads to a direct modal approximation in which the thermodynamic forces appear in a coupled way. Finally, the number of internal variables of the reduced model is no more than the size of the orthogonal basis used for the inelastic deformation tensors and, therefore, guarantees an excellent order reduction.

2.3 Modal basis of a slender structure

A slender structure is often represented as a beam, subject to elongation and different possible curvatures. The description of its movement is limited to the displacement of the neutral fiber. In this case, only are necessary the displacements of all the grids and nozzles, represented in Fig. 2.

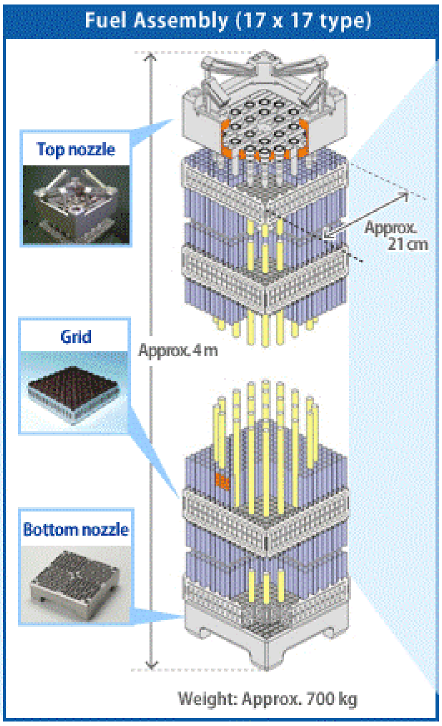

Fig. 2. Components of a PWR fuel assembly (Pramuditya, 2009).

That is why the averaged displacement $\boldsymbol{U}^a(g,t)$ of any grid g is first described, where $S(g)$ is the surface of the grid number g and Ng is the maximum number of grids and nozzles in the FA.

$$\boldsymbol{U}^a(g,t) = \frac{1}{S(g)} \iint_{x\in g} \boldsymbol{u}(x,t)dS\,, \forall g \in [1, Ng] \qquad (8)$$

Practically it means that the support of the macroscopic displacement modes is a line of Ng nodes ($Ng = 12$ for 2 nozzles and 10 grid), see Fig. 3 for an example with 3 grids. Accordingly, in a 3D space, a maximum of 36 modes is then sufficient to project all the possible deformed shapes of such a line with 12 points.

Of course, a smaller basis is valued if it is relevant. In order to construct such an optimal basis of displacement modes, it is then natural to apply a Karhünen-Loeve transformation (Karhunen, 1946), also called Proper Orthogonal Decomposition (Sirovich, 1987), on a representative set of deformation results expressed on the support of the displacement modes (here, the 12-nodes line). They might be obtained from in situ measurements, when possible and from detailed calculations otherwise.

Finally is obtained an orthonormal basis of J displacement modes $\boldsymbol{U}_j^a$ supported by a line of Ng nodes. It enables to decompose the averaged displacement of the grids g at instant t into a collection of orthogonal modes:

$$\begin{cases} \boldsymbol{U}^a(g,t) \approx \displaystyle\sum_{j=1,J} \alpha_j^a(t)\, \boldsymbol{U}_j^a(g) \\ (\boldsymbol{U}_k^a, \boldsymbol{U}_l^a) = \displaystyle\sum_{1}^{Ng} \boldsymbol{U}_k(g).\boldsymbol{U}_l(g) = \delta_{kl}, \forall (k,l)\epsilon[1,J]^2 \\ J = argmin_L \left(\dfrac{\sum_{k=1}^{L} \lambda_k}{\sum_{k=1}^{k\_max} \lambda_k} \geq 1 - \rho \right) \end{cases} \qquad (9)$$

with λ_k the eigenvalue of the grid displacement correlation matrix and ρ a given tolerance.

As seen in section 5, the local scalar product used for displacements can be weighted in order to decrease the relative influence of the axial displacement.

Following the NTFA method, the inelastic strain tensor field are developed on an orthonormal basis of I space functions $\boldsymbol{\varepsilon}_i^{in}$ $(1 \leq i \leq I)$, called inelastic modes, where each mode is a deviatoric symmetric tensor of order 2:

$$\begin{cases} \boldsymbol{\varepsilon}^{in}(x,t) \approx \displaystyle\sum_{i=1,I} \alpha_i^{in}(t)\, \boldsymbol{\varepsilon}_i^{in}(x) \\ \left(\boldsymbol{\varepsilon}_p^{in}, \boldsymbol{\varepsilon}_q^{in}\right) = \displaystyle\iiint_{x\in\Omega} \boldsymbol{\varepsilon}_q^{in}(x) : \boldsymbol{\varepsilon}_q^{in}(x) dV = \delta_{pq} \end{cases} \qquad (10)$$

Above, $\boldsymbol{\varepsilon}_i^{in}$ is the ith inelastic tensorial mode of the basis and $\alpha_i^{in}(t)$, its scalar magnitude at time t. As well as for the displacement modes, this basis of inelastic modes can be determined by a snapshot POD applied on a collection of inelastic strain fields obtained with the detailed model.

2.4 Mechanical fields associated to the different modes

It is now necessary to determine the elastic and inelastic strain fields and the stress field associated to the different modes. For this, each mode is applied to the detailed model as an elementary loading and, then, identify the associated stress and strain fields.

For the macroscopic displacement modes, the averaged grid displacement $\boldsymbol{U}_j^a$ is imposed at the boundaries of the slender structure, assuming that it behaves elastically ($\boldsymbol{\varepsilon}^{in} = 0$). The goal is to characterize the elastic response of the FA to any external loadings, decomposed on the displacement basis, and to identify the associated local stress and strain fields, as well as the resulting forces. This is achieved by solving the system of equations (11) with the detailed model of the system, where $\boldsymbol{\sigma}$ and $\boldsymbol{\varepsilon}$ are the stress and strain tensors**,** respectively, $\mathbb{L}$ is the 4th order tensor of elasticity, S_g is the surface of the grid number g and $\boldsymbol{U}^a(g)$, its averaged displacement.

$$\begin{cases} div\boldsymbol{\sigma} = 0 \\ \boldsymbol{\sigma} = \mathbb{L}:\boldsymbol{\varepsilon} \\ \boldsymbol{U}_j^a(g) = \dfrac{1}{S_g}\displaystyle\iint_{x\in g} \boldsymbol{u}(x)dS \ \forall g = 1, Ng \\ \boldsymbol{\varepsilon}^{in} = 0 \end{cases} \tag{11}$$

The solution enables to identify, at any point of the detailed model:

- $\boldsymbol{\sigma}_j^{a\_asso}$, the stress field associated to the elastic response of the FA to the macroscopic displacement mode *j*,
- $\boldsymbol{\varepsilon}_j^{a\_asso}$, the associated strain field,
- $\boldsymbol{U}_j^{a\_asso}$, the associated displacement field.

For the inelastic strain modes, the same type of operation is done. The difference is that zero displacement is maintained at the boundary of the slender structure (averaged displacement of the grids $\boldsymbol{U}^a(g)$ blocked) while imposing an inelastic strain $\boldsymbol{\varepsilon}_i^{in}$. The corresponding local detailed elementary problems writes:

$$\begin{cases} div\boldsymbol{\sigma} = 0 \\ \boldsymbol{\sigma} = \mathbb{L}:(\boldsymbol{\varepsilon} - \boldsymbol{\varepsilon}^{in}) \\ \boldsymbol{U}^a(g) = \dfrac{1}{S_g}\displaystyle\iint_{x\in g} \boldsymbol{u}(x)dS = 0 \ \forall g = 1, Ng \\ \boldsymbol{\varepsilon}^{in} = \boldsymbol{\varepsilon}_i^{in} \end{cases} \tag{12}$$

The solution enables to identify, at any point of the detailed model:

- $\boldsymbol{\sigma}_i^{in\_asso}$, the stress field associated to the elastic response of the FA to the inelastic mode $\boldsymbol{\varepsilon}_i^{in}$,
- $\boldsymbol{\varepsilon}_i^{in\_asso}$, the associated strain field,
- $\boldsymbol{U}_i^{in\_asso}$, the associated displacement field.

Thanks to the linearity of the elasticity operator $\mathbb{L}$, one can sum these elementary solutions. The local state of the system then appears as a linear combination of the aforementioned associated fields:

$$\boldsymbol{\sigma}(x,t) = \sum_{i=1,I} \alpha_i^{in}(t)\, \boldsymbol{\sigma}_i^{in\_asso}(x) + \sum_{j=1,J} \alpha_j^{a}(t)\, \boldsymbol{\sigma}_j^{a\_asso}(x) \tag{13}$$

$$\boldsymbol{\varepsilon}(x,t) = \sum_{i=1,I} \alpha_i^{in}(t)\, \boldsymbol{\varepsilon}_i^{in\_asso}(x) + \sum_{j=1,J} \alpha_j^{a}(t)\, \boldsymbol{\varepsilon}_j^{a\_asso}(x) \tag{14}$$

$$\boldsymbol{U}(x,t) = \sum_{i=1,I} \alpha_i^{in}(t)\, \boldsymbol{U}_i^{in\_asso}(x) + \sum_{j=1,J} \alpha_j^{a}(t)\, \boldsymbol{U}_j^{a\_asso}(x) \tag{15}$$

By replacing $\boldsymbol{\sigma}$ with its modal expression in the principle of virtual power, and successively choosing all the J displacement modes $\boldsymbol{U}_p^{a\_asso}$ as virtual displacement, shows that each internal force f_p^{int}, identified as the projection of stresses onto $\boldsymbol{\varepsilon}_p^{a\_asso}$, must balance the external force f_p^{ext}, projection of the external forces onto mode $\boldsymbol{U}_p^a$.

$$\begin{cases} f_p^{int} = f_p^{ext}, \forall p \epsilon [1, J] \\ f_p^{int} = \sum\limits_{i=1,I} \alpha_i^{in} \iiint\limits_{x\in\Omega} \boldsymbol{\sigma}_i^{in\_asso} : \boldsymbol{\varepsilon}_p^{a\_asso} dV + \sum\limits_{j=1,J} \alpha_j^{a} \iiint\limits_{x\in\Omega} \boldsymbol{\sigma}_j^{a\_asso} : \boldsymbol{\varepsilon}_p^{a\_asso} dV \\ f_p^{ext} = \iint\limits_{x\in\partial\Omega} \boldsymbol{P}^{ext} . \boldsymbol{U}_p^{a\_asso} dS + \iiint\limits_{x\in\Omega} \boldsymbol{f}^{vol} . \boldsymbol{U}_p^{a\_asso} dV \approx \sum\limits_{g=1}^{Ng} \boldsymbol{F}^{ext}(g) . \boldsymbol{U}_p^a(g) \end{cases} \qquad (16)$$

Above, $\boldsymbol{P}^{ext}$ is the mechanical loading applying on the FA in the reactor core due to contact between FA, fluid pressure or drag forces, and $\boldsymbol{f}^{vol}$ are volume forces such as gravity. It is worth noting that the external forces are often aggregated at each nozzle/grid level. So, in practice, one can directly apply the scalar product between these external forces $\boldsymbol{F}^{ext}$ and the boundary average displacement $\boldsymbol{U}_p^a$ to obtain the J external modal forces f_p^{ext}.

In the end, the force equilibrium (16) gives a linear system of J equations with the reduced state variables α_i^{in} and α_j^a. Therefore, this system must be completed by I independent equations that derived from the constitutive equations in the two following sections.

2.5 Thermodynamic forces

I thermodynamic forces β_p^{in} are defined as the conjugate of the inelastic strains $\boldsymbol{\varepsilon}_p^{in}$ when computing the total dissipation.

$$P^{dissipation} = \sum_{p=1}^{I} \beta_p^{in} \dot{\alpha}_p^{in} = \iiint\limits_{x\in\Omega} \boldsymbol{\sigma} : \dot{\boldsymbol{\varepsilon}}^{in} dV \qquad (17)$$

Getting $\dot{\boldsymbol{\varepsilon}}^{in}$ from (10) and replacing $\boldsymbol{\sigma}$ by (13), this thermodynamic force appears as an explicit linear function of the reduced state variables α_i^{in} and α_j^a at time t.

$$\beta_p^{in} = \iiint\limits_{x\in\Omega} \boldsymbol{\sigma} : \boldsymbol{\varepsilon}_p^{in} dV = \sum_{i=1,I} \alpha_i^{in} \iiint\limits_{x\in\Omega} \boldsymbol{\sigma}_i^{in\_asso} : \boldsymbol{\varepsilon}_p^{in} dV + \sum_{j=1,J} \alpha_j^{a} \iiint\limits_{x\in\Omega} \boldsymbol{\sigma}_j^{a\_asso} : \boldsymbol{\varepsilon}_p^{in} dV \qquad (18)$$

Here β_p^{in} appears as the local stress projection (19) onto the inelastic strain mode $\boldsymbol{\varepsilon}_p^{in}$, very similar but not exactly equal to the reduced stress σ_k of the NTFA defined in (4).

2.6 Reduced evolution law

Let us consider a Norton creep law (19), whose flow velocity depends on a power law of the stress.

$$\begin{cases} \boldsymbol{\sigma} = \dfrac{\partial w}{\partial \boldsymbol{\varepsilon}} = \mathbb{L} : (\boldsymbol{\varepsilon} - \boldsymbol{\varepsilon}^{vp}) \\ \psi(\boldsymbol{\sigma}) = a\, \sigma_{eq}^{m} \\ \dot{\boldsymbol{\varepsilon}}^{vp} = \dfrac{\partial \psi}{\partial \boldsymbol{\sigma}} = \dfrac{3}{2} m a \sigma_{eq}^{m-1} \dfrac{\sigma'}{\sigma_{eq}} \end{cases} \qquad (19)$$

The purpose is to determine the values of the modal rates $\dot{\alpha}_i^{in}$ for any state of the reduced system characterized by the values of α_i^{in} and α_j^{a}. Now that the modal forces $\beta_p^{in}$are explicitly determined, similarly to (Michel and Suquet 2003) and (Michel and Suquet 2004), the aim is to use these reduced forces to directly express the evolution of the reduced internal variables. Wishing to do like Michel and Suquet in the projection of the evolution law onto the mode $\boldsymbol{\varepsilon}_i^{in}$, when they suggested to replace σ_{eq} in (5) by s_r (6), the norm of the reduced stresses of the r phase. By analogy, based on the normalization (10), we propose:

$$\begin{cases} \dot{\alpha}_i^{vp} = \iiint \dot{\boldsymbol{\varepsilon}}^{in} : \boldsymbol{\varepsilon}_i^{in} dV \approx \iiint \dfrac{3}{2} \dfrac{\partial \psi}{\partial \sigma_{eq}} \dfrac{\boldsymbol{\sigma}' : \boldsymbol{\varepsilon}_i^{in}}{s_r} dV \\ s_r = \|\boldsymbol{\beta}^{in}\| \dfrac{1}{V} \sqrt{\dfrac{2}{3}} \\ \|\boldsymbol{\beta}^{in}\| = \sqrt{\displaystyle\sum_{i=1}^{I} {\beta_i^{in}}^2} \end{cases} \tag{20}$$

Applied to the Norton creep law, and now considering that the creep characteristic $a(x)$ is no longer homogeneous, the reduced evolution law becomes (21).

$$\begin{cases} \dot{\alpha}_i^{vp} = a_i \, \|\boldsymbol{\beta}^{in}\|^{m-1} \dfrac{\beta_i^{in}}{\|\boldsymbol{\beta}^{in}\|} \\ \|\boldsymbol{\beta}^{in}\| = \sqrt{\displaystyle\sum_{i=1}^{I} {\beta_i^{in}}^2} \end{cases} \tag{21}$$

The modal characteristic a_i is a function of the local creep characteristic a and depends on the volume V as detailed in the next section. Lest us observe that this relation takes a variational form in the reduced basis, with a dissipative function $\psi_r(\boldsymbol{\beta}^{vp})$ defined by:

$$\begin{cases} \dot{\boldsymbol{\alpha}}^{in} = \dfrac{\partial}{\partial \boldsymbol{\beta}} \psi_r(\boldsymbol{\beta}^{vp}) \\ \psi_r(\boldsymbol{\beta}^{vp}) = \left\| \displaystyle\sum_{i=1}^{I} a_i {\beta_i^{in}}^2 \right\|^{m/2} \end{cases} \tag{22}$$

The reduced potential ψ_r is not an intensive potential but an extensive one, controlling the total dissipation of the phase considered in the structure. In addition, ψ being a convex scalar function, $\psi_r(\boldsymbol{\beta}^{vp})$ is a lower bound of the exact integral of the potential over the volume of the considered phase.

$$\psi_r(\boldsymbol{\beta}^{vp}) = V\psi(s_r) \leq \iiint\limits_{x \in \Omega} \psi\big(\sigma_{eq}(x)\big) dV \tag{23}$$

In practice, vector $\boldsymbol{\beta}^{in}$ (18) is composed of I components which are linear combinations of the $I + J$ state variables with precomputed coefficients. Again, the greatest interest of the method lies in the fact that this evolution of the internal variables is calculated only once for the full structure, just as if there were only one integration point.

2.7 Handling local heterogeneity

Usually in classical homogenization, the RVE is small and the influent factors such as temperature are homogeneous at this scale. In the present case, the RVE is a large structure that undergoes spatial variations of temperature $T(x)$ and neutron flux $\Phi(x)$. Consequently, the material characteristics are heterogeneous. This is particularly the case for the creep characteristic $a(x)$, which depends strongly on the local fast neutron flux that is more intense in the middle of the FA than at its extremities. One should also note that these characteristics are subject to evolution over time, thus might need an update at a proper frequency. Therefore, the modal characteristics a_i of (21) must be determined in accordance with these parameters at current time t and in relation with the spatial distribution of the considered mode.

A first technique is to evaluate a_i in the particular case of a stress field $\boldsymbol{\sigma} = \boldsymbol{\varepsilon}_i^{in}$ aligned with mode i. This generates a thermodynamic force $\beta_i^{in} = 1$, oriented exactly in the i^{th} direction $(\beta_{j\neq i}^{in} = 0)$. When equalizing in this case the reduced and full dissipations in (24):

$$ma_i = \iiint_{x\in\Omega} \boldsymbol{\varepsilon}_i^{in} : (\frac{3}{2} am \left(\sqrt{\frac{3}{2}\boldsymbol{\varepsilon}_i^{in} : \boldsymbol{\varepsilon}_i^{in}}\right)^{m-2} \boldsymbol{\varepsilon}_i^{in}) dV \qquad (24)$$

which leads to:

$$a_i = \iiint_{x\in\Omega} a \left(\sqrt{\frac{3}{2}\boldsymbol{\varepsilon}_i^{in} : \boldsymbol{\varepsilon}_i^{in}}\right)^{m} dV \qquad (25)$$

Eq. (25) clearly shows how the local characteristic a, variable in space and time, is weighted by the local amplitude of mode $\boldsymbol{\varepsilon}_i^{in}$ through the Norton potential. One can notice that, even when a is homogeneous, this modal characteristic is possibly different from a and provides a correction to the reduced evolution law (21).

A second technique for evaluating a_i is to consider instead $\dot{\alpha}_i^{vp} = 1$, that is a strain rate field of the form $\dot{\boldsymbol{\varepsilon}}^{in} = \boldsymbol{\varepsilon}_i^{in}$. A direct calculation of dissipation in a reduced basis yields then :

$$P^{dissipation} = \beta_i^{in}\dot{\alpha}_i^{in} = \beta_i a_i m \beta_i^{m-1} \qquad (26)$$

that is:

$$ma_i = \beta_i^{1-m} = P^{dissipated^{1-m}} \qquad (27)$$

Calculating the local dissipation $ma\sigma_{eq}^{m}$ from the flow rule (20) used with $\dot{\boldsymbol{\varepsilon}}^{in} = \boldsymbol{\varepsilon}_i^{in}$ yields then:

$$a_i = \left[\iiint a^{1/(1-m)} \left(\sqrt{\frac{2}{3}\boldsymbol{\varepsilon}_i^{in} : \boldsymbol{\varepsilon}_i^{in}}\right)^{\frac{-m}{1-m}} dV\right]^{1-m} \qquad (28)$$

The approximate modal characteristics (25) and (28) arise from imposed stress or strain rate fields that are possibly more prescriptive than reality. Thus, they constitute bounding values. These bounds become closer one from another when a becomes homogeneous over the structure. Moreover, they are exactly equal in the particular case of linear homogeneous creep ($a = constant, m = 2$). Of course, one can take the geometric average of these two bounds for a better assessment.

2.8 Reduced problem and solution algorithm

From the force balance equation, the state deduced thermodynamic forces β and the above approximate evolution law of the modal rates $\dot{\alpha}_i^{in}$ lead to our reduced order model of FA:

$$\begin{cases} \left(D_{balance}.\boldsymbol{\alpha}\right)_p = \displaystyle\sum_{g=1}^{Ng} \boldsymbol{F}^{ext}(g).\boldsymbol{U}_p^a(g), \forall p \epsilon [1,J] \\ \boldsymbol{\beta}^{in} = D_{creep}.\boldsymbol{\alpha} \\ \dot{\alpha}_i^{vp} = a_i \, \|\boldsymbol{\beta}^{in}\|^{m-1} \dfrac{\beta_i^{in}}{\|\boldsymbol{\beta}^{in}\|} \quad with \; \|\boldsymbol{\beta}^{in}\| = \sqrt{\displaystyle\sum_{i=1}^{I} {\beta_i^{in}}^2} \end{cases} \tag{29}$$

with the unknown vector $\boldsymbol{\alpha}$ and influence matrices $D_{balance}$, D_{creep} given by:

$$\begin{cases} \boldsymbol{\alpha} = \left(\alpha_1^a, \dots, \alpha_J^a, \alpha_1^{in}, \dots, \alpha_I^{in}\right)^t \\ D_{creep_{ik}} = \displaystyle\iiint_{x\in\Omega} \boldsymbol{\sigma}_k^{asso} : \boldsymbol{\varepsilon}_i^{in} dV, \forall k \in [1, J+I], \forall i \in [1, I] \\ D_{balance_{jk}} = \displaystyle\iiint_{x\in\Omega} \boldsymbol{\sigma}_k^{asso} : \boldsymbol{\varepsilon}_j^{a\_asso} dV, \forall k \in [1, J+I], \forall j \in [1, J] \end{cases} \tag{30}$$

The reduced problem (29) is a conventional quasi-static creep problem that can be solved by different methods. The authors chose a simple prediction-correction algorithm to solve the equilibrium at the different calculation times, which are taken identical to those used for the reference model. First, the prediction is computed by solving the linear system defined by matrix $D_{balance}$ restricted to the α_j^a unknowns, noted K, and the external forces projected on the displacements basis. Second, the correction phase consists in solving the reduced evolution law. For this, an implicit Runge-Kutta algorithm is used to integrate creep over the time step. These two operations are repeated until convergence of the relative force residue under a prescribed value of 10^{-4}. Since K is inverted only once and stored, this method is usually fast except when the inelastic deformation becomes large. When the convergence is too slow, a Richardson method (Richardson and Glazebrook, 1911) is used to provide an acceleration almost comparable to that of the Newton-Raphson method.

3. Validation on a simple case study with non-linear creep

3.1 Description of the reference model

This section presents the results of a first application of our model to a simple slender structure. The structure considered for the case study is represented by its finite element mesh in Fig. 3. It represents a simplified skeleton model of a FA. The structure is made of a base and of 3 grids connected together by 4 vertical legs of square section. It is 3m high, 0.4m wide. The thickness of the legs, base and last grid is 0.05m. The thickness of grid 1 and grid 2 is doubled to 0.1m. The reference mesh contains 2136 hexahedral quadratic finite elements and 14748 nodes.

The possible load cases are external forces applied either on grid 1, 2 or 3, or on a combination of them. The forces remain constant in all load cases, which duration is 10^8 seconds, similar to the total irradiation duration of a FA. Forces are distributed homogeneously on each grid and oriented in the 3 space directions. Concerning the boundary conditions, the lower face of the base is fixed to the ground.

The constitutive law is elastic and viscoplastic following a Norton law (19) with a stress exponent equal to 1.4 ($m = 2.4$), as frequently proposed for irradiation secondary creep of Zirconium alloys (Fidleris, 1988; Gharbi, 2015) in PWR conditions. The creep parameter a is arbitrary fitted to generate creep strains of the same order of magnitude as those affecting the guide thimbles of the FA in a PWR.

Table 1: material characteristics for the test case.

Norton creep law	Young modulus Pa	Poisson coefficient ν	Creep sensitivity a	Stress exponent N
$\dot{\varepsilon}_{eq} = a\sigma_{eq}^{N}$	10^{10}	0.3	4.10^{-21}	1.4

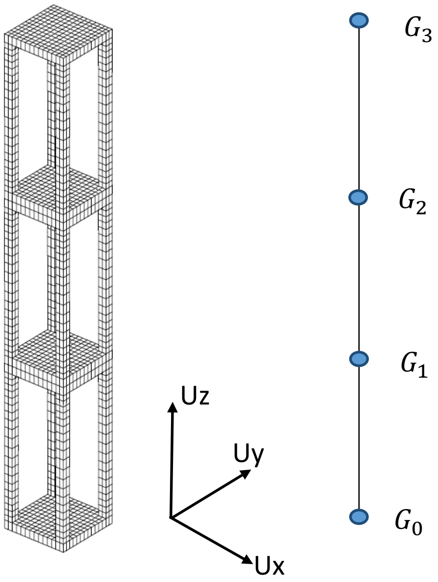

Fig. 3. Mesh of the simplified fuel assembly defined for the case study (left) and symbolic line supporting the boundary displacement modes of the reduced model (right).

3.2 ROM identification

3.2.1 Displacements modes and associated fields

In order to build the ROM, the first operation to conduct is to identify the displacement modes of the case study. As exposed in paragraph 3.2, only the mean displacement of each grid are looked for. Considering this, a line made of 4 nodes is defined: G_0, G_1, G_2 and G_3 (see Fig. 1). Node G_0 represents the basis and remains motionless. Nodes G_1, G_2 and G_3 represent the grids.

Here, a numerical characterization of the displacement modes is unnecessary since the canonical basis of all the displacements modes $\boldsymbol{U}_j^a$ consists in only three vectors: 3 grids × 3 translations. The first three modes are thus the unit displacement of G_1 according to Ux, Uy and Uz, respectively, with no displacement on G_2 and G_3. The other six modes are obtained by permuting the roles of G_1 with G_2 and G_3, respectively.

For each displacement mode $\boldsymbol{U}_j^a$, the determination of the three associated fields $\boldsymbol{\sigma}_j^{a\_asso}$, $\boldsymbol{\varepsilon}_j^{a\_asso}$, $\boldsymbol{U}_j^{a\_asso}$ requires the resolution of only one elastic problem, with a fixed base, the modes $\boldsymbol{U}_j^a$being applied to the grid nodes of G_1, G_2, G_3, respectively. Eq. (12) provides the necessary relation to transfer this Dirichlet condition onto the detailed model's mesh by means of Lagrange multipliers. The nine associated $\boldsymbol{U}_j^{a\_asso}$ modes obtained are displayed on Fig. 4.

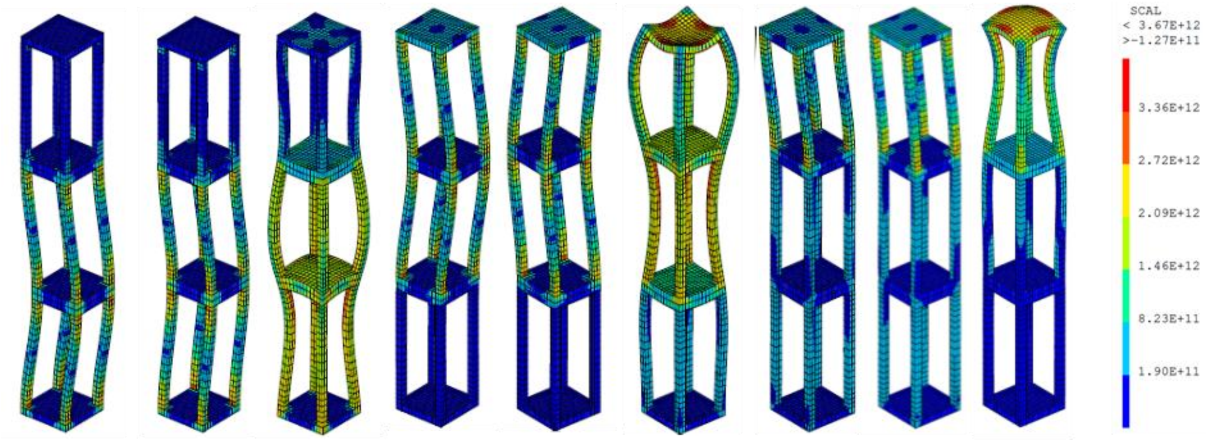

Fig. 4. Elastic mode shapes $\boldsymbol{U}_j^{a\_asso}$ *(x10*$^{-2}$*) associated to the 9 macroscopic displacement modes* $\boldsymbol{U}_j^{a}$ *controlling the lateral and vertical average grid displacements. Isovalues are for the corresponding Von Mises stress fields (Pa).*

3.2.2 Inelastic modes and associated fields

The characterization of the creep behavior of this structure is approached by applying different load cases to the reference model described in 3.1. For this purpose, a small number of numerical experiments, namely 11 creep calculations were run with arbitrarily imposed grid forces, chosen to project on the 9 displacement modes $\boldsymbol{U}_j^{a}$ in a linearly independent manner. Fig. 5 shows the amplified deformed shapes obtained at the end of these creep calculations. The final inelastic strain fields obtained form a collection of snapshots. The identification of the inelastic strain modes is operated thanks to a proper orthogonal decomposition (POD) on these snapshots. Of course, out of the context of this simple test, a more complex non-linear behavior law would require more load cases to explore the space of the creep fields generated by external varying forces on grids.

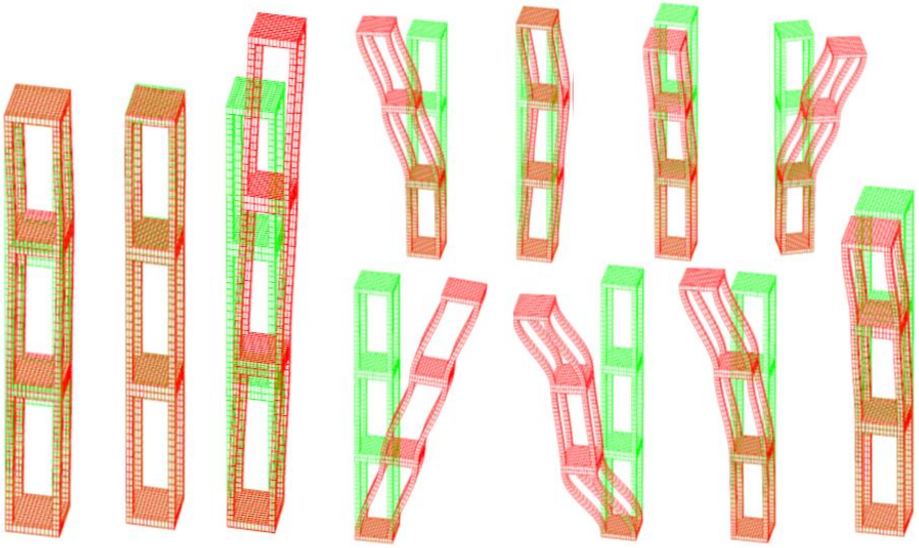

Fig. 5. Final static deformed shape (x50) of the case study when submitted to 11 arbitrary load cases defined to characterize its creep response and later identify dominant inelastic modes by means of a POD made on these snapshots.

Since the number of snapshots realized was relatively small compared to the number of displacement modes $\boldsymbol{U}_j^{a}$, it was chosen arbitrarily not to restrain the quality of the POD basis and kept 10 modes to build the reduced basis of inelastic strains. Of course, a higher number of snapshots would better characterize the creep behavior of the case study.

The associated fields $\boldsymbol{\sigma}_i^{in\_asso}$, $\boldsymbol{\varepsilon}_i^{in\_asso}$ and $\boldsymbol{U}_i^{in\_asso}$ then come as the solutions of the elastic problems, defined by (16).

3.3 Comparison of reference and reduced model solutions

In order to evaluate the identified reduced model, a new arbitrary load case is computed. It is designed to be significantly different from the loadings of the snapshots used to identify the inelastic strains basis. For example, one can consider a random linear combination of these previous loadings. Table 2 presents the values of the forces applied during a period of 10^8 seconds on the three grids for this load case.

Table 2: values of the forces applied on the grids for the test case of evaluation of the reduced model.

Applied forces (N)	Fx	Fy	Fz
Grid 1	543	-247	200
Grid 2	0	682	400
Grid 3	-321	-90	300

Fig. 6. presents the time-evolution of the creep modal amplitudes of the ROM and Fig. 7 presents the deformed shapes of the case study for the reduced and the reference models, which superpose quite well. This last figure fairly shows the good agreement between the two models.

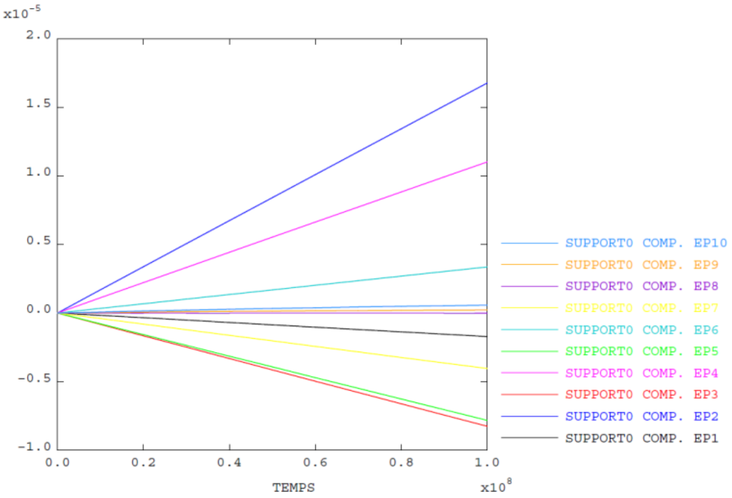

Fig. 6. Time evolution of the 10 creep amplitudes over 10^8 s of constant loading.

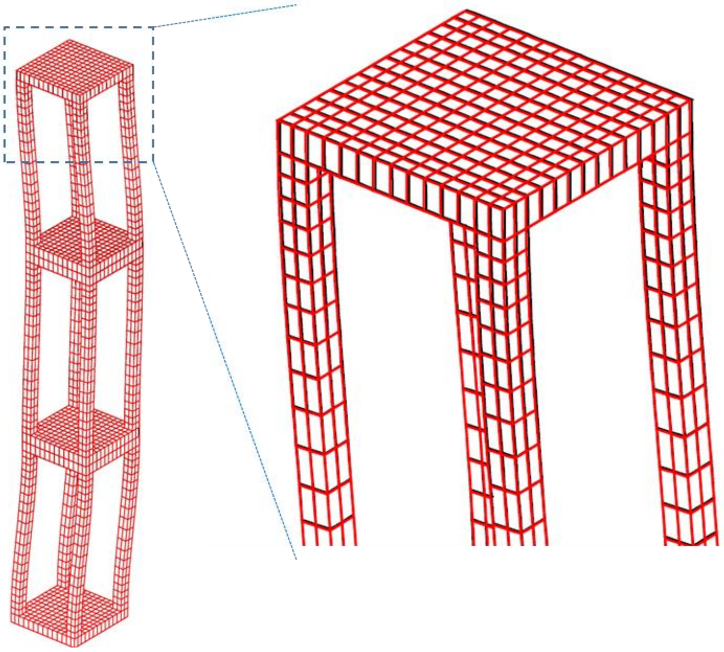

Fig. 7. Superposition of the final deformed shapes for the reference (black lines) and reduced model (red lines).

The final displacements of the grids are recorded and compared in table 3. Their time-evolution in Fig. 8 shows that the reduced elastic matrix gives a good prediction and that the final relative error on the displacements is due to the approximation of the creep law in the reduced model. This prediction level in a creep simulation is comparable to that originally obtained by the NTFA authors for an elastoplastic bending, see (Michel and Suquet, 2004).

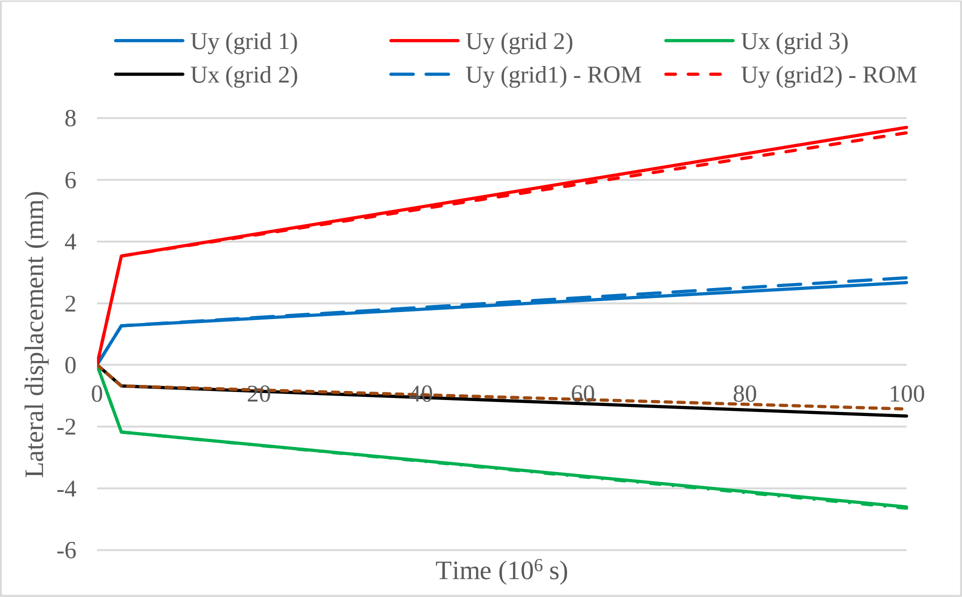

Fig. 8. Comparison of the time – displacement curves of the grids between the reference model (solid line) and the ROM (dashed line).

Table 3: comparison of the displacements of the grids between the ROM and the reference model.

	Ux (ref.) / Ux (ROM)	Relative error Ux	Uy (ref.) / Uy (ROM)	Relative error Uy
Grid 1	1.40/1.37mm	-2,2%	2.67/2.83mm	6%
Grid 2	-1.66/-1.43mm	-13,8%	7.70/7.53mm	-2,2%
Grid 3	-4.60/-4.64mm	0,8%	7.66/7.48mm	-2,3%

Table 4 presents the computing time for the load case defined in table 2. The reference and the reduced models use identical time discretization, which includes 11 time steps. The results show that the reduced model is more than 100 times faster than the reference one, a finite element model using (CEA, 2020). This speed-up was obtained for a small size test simulation and it is expected to maintain or to improve this speed up with larger simulations involving many FA.

Table 4: typical computing time (1 processor).

Reference model (Cast3M)	ROM: 9 displacement modes / 10 creep modes
41953ms	359ms

4. Creep of a PWR FA in heterogeneous conditions

In the previous section, a simple case showed that the NTFA is transposable to a slender RVE and confirms the expected speed-up. The objective is now to apply it to our industrial target, which is a FA, whose reference model has a larger size and is far more complex. First, unlike the previous example using only massive finite elements, our reference model for the FA uses pipe generalized finite elements for the rods or guide-tubes, and shell elements for the grids. This imposes an adaptation of the operators to the generalized coordinates. Second, contrary to the homogenization approach, the creep characteristic $a(x)$

becomes heterogeneous, since it depends on the fast neutron flux, which is itself heterogeneous and slightly variable with time. Finally, the structure is multiphase, with some areas of the structure not creeping at all, such as the massive steel nozzles that are located outside the neutron flux.

4.1 Reference model

Considering a FA whose dimensions and characteristics are close to, but different from, those of the French 1300MW PWR FA. The FA has a total height of about 5 m and a width of 21 cm. It includes 10 square grids of 17x17 cells. There are 24 guide thimbles and the 265 rods are pinched by small leaf springs at the passage of each grid. The upper and lower nozzles are made of steel and are connected to the guide thimbles by rigid links.

The discretization for rods and guide thimbles uses generalized pipe elements (beam with parameters corresponding to an annular section). The grids and the end caps are represented by shells while all the connections use discrete elements similar to springs.

The goal here is to validate the model reduction for creep, the other phenomena will be integrated later. Therefore, focusing in this study on the creep of the rods and guide thimbles. The relaxation of the grid springs is not taken into account. Similarly the contacts between rods and grid are kept closed in all circumstances and sliding is forbidden. Moreover, the mechanical influence of the presence of fuel pellets is deliberately neglected whatever the burn-up of the rods.

The behavior law adopted for the rods and the guide thimbles is the irradiation creep law used in FRAPCON 3.4 (Geelhood et al., 2011), recalled in table 5, with $\emptyset$ denoting the fast neutron flux.

Table 5: irradiation creep law parameters.

Irradiation creep law	$C_0\ (nm^{-2}s^{-1})^{-C1}MPa^{-C2}$	C_1	C_2	$f(T)$
$\dot{\boldsymbol{\varepsilon}}^{creep} = C_0\emptyset^{C_1}{\sigma_{eq}}^{C_2}f(T)$	1.874E-24	0.85	1	-3.18562+0.00699T

The boundary conditions are defined to represent the mechanical conditions in a PWR core. They consist in blocking the base of the bottom nozzle and in prescribing an axial guidance of the top nozzle. The mechanical loadings are a constant axial compression force of 5000N applied by the holdown system on the top nozzle, together with axial or transverse forces distributed on the grids (hydraulic forces and possible contact force with a neighbor FA). As for the fast neutron flux, a maximum intensity of $\emptyset = 0.8\ 10^{18} nm^{-2}s^{-1}$ in the middle of the FA is considered, with a conventional decrease to zero when reaching the nozzles, see Fig. 9. A lateral gradient of neutron flux is also applied for the external positions in the core.

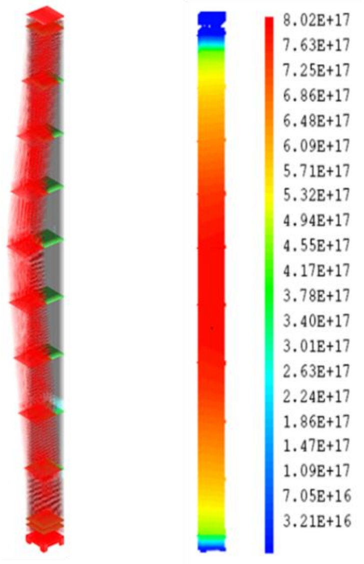

Fig. 9. Deformed (red) and undeformed (green) mesh of a FA, fast neutron flux (>1MeV) (n/m².s).

4.2 Parameter space and design of numerical experiments

In order to construct the macroscopic and inelastic modes, the priority is to define the parameter space describing the different loadings and then construct a reasonable filing using detailed model realizations. For a given FA design, the main parameters that influence the deformation are the lateral forces that apply on the grids and their vicinity, as well as the position of the assembly in the core. Indeed, an assembly positioned in the center of the core presents a power distribution that varies only in the vertical axis, see Fig. 9, while a FA at the outer edge of the core also undergoes a significant lateral flux gradient. The outer face of such a FA commonly has a flux approximately twice as low as the one facing the core.

For the hydraulic forces applied to the FA, in order to synthesize the information, the geometry is divided into 10 zones, each encompassing a grid and segments of rods and guide thimbles on either side of the grid. The sum of all the hydraulic and contact forces in a zone constitutes a mechanical loading brought back on the grid. Table 6 gives the different profiles LAT1 to LAT9 defined to study the response of the FA under lateral loading. LAT1, LAT2, LAT3 and LAT5 are realistic sets of forces coming from hydraulic simulations (De Lambert et al., 2021). LAT4 figures a contact force at mid height without hydraulic lateral forces. LAT6 to LAT9 are purely hypothetic sets of lateral forces added to complete the representation of the forces up to mode 5, also to represent possible contacts with a neighbor FA at different heights. Forces beyond mode 5 are considered unlikely and are not observed during measurements on deformed assemblies (Andersson et al., 2005; Gabrielsson et al., 2018).

Table 6: 9 lateral force fields (N) to be applied on the 10 grids of a FA in the detailed simulations.

Grid	LAT1	LAT2	LAT3	LAT4	LAT5	LAT6	LAT7	LAT8	LAT9
1	-30	0	90	0	0	0	0	-100	-100
2	-72	-5	60	0	-20	0	-100	0	0
3	-150	20	30	0	-40	-100	0	100	100
4	-30	70	0	0	-100	0	0	0	0
5	36	100	0	0	-30	0	100	0	-100
6	18	45	0	150	0	0	0	-100	0
7	9	25	0	0	20	100	0	0	100

8	0	10	0	0	80	0	-100	0	0
9	0	3	30	0	20	0	0	100	-100
10	0	0	60	0	0	0	0	0	0

A test plan has been designed for the construction of the different modal basis. It is built with three types of detailed reference calculations.

The first part of the test plan is the most consequent. It considers a FA in a central position (most of the FA are defined as such), meaning that the neutron flux is homogeneous in any horizontal section. Using the force profiles of table 6, 68 combinations of lateral forces for X and Y directions are computed with the FA detailed model.

The second part of the test plan considers a FA positioned outside, on the west side. This means that the FA is subject to a neutron flux gradient in the X direction. Lateral forces of table 6 are only applied in this direction because the feedback shows that the deformations are more pronounced in the core radial direction. Moreover, an information on the coupling effects induced by combination of lateral forces in different directions was already obtained in the first part of the test plan, although not with the same neutron flux.

The last part of the test plan copies the second one but considers a FA in the north external position, *i.e.* with a rotation of 90 degrees of the mechanical and neutron flux loadings.

4.3 Scalar product adaptation for beam and pipe generalized elements

To construct the inelastic modes, a POD is applied on the inelastic strain snapshots using the scalar product (31).

$$\left(\boldsymbol{\varepsilon}_p^{in},\boldsymbol{\varepsilon}_q^{in}\right)=\iiint\limits_{x\in\Omega}\boldsymbol{\varepsilon}_q^{in}(x):\boldsymbol{\varepsilon}_q^{in}(x)dV \qquad (31)$$

However, within generalized elements of the pipe or Euler beam type, inelastic deformations are only accessible in the form of generalized deformations of axial strain $E1$, curvatures $C2$, $C3$. It is therefore necessary to express the local deformations at any point x of the beam or pipe section in terms of these generalized deformations, before integrating them over the volume of the element. The point x is characterized by its radius $r(x)$ and its angular position $\theta(x)$ in the section. The creep deformation being considered isochoric, a Poisson's ratio $\nu = 0.5$ is introduced, and after neglecting the shear strain, it is possible to construct an underlying 3D strain tensor as:

$$\begin{cases}\varepsilon_{axial}(x) = E1 + r(x)cos\theta(x)C3 + r(x)sin\theta(x)C2 \\ \boldsymbol{\varepsilon}(x) = \begin{bmatrix}-0.5 & 0 & 0\\ 0 & -0.5 & 0\\ 0 & 0 & 1\end{bmatrix}\varepsilon_{axial}(x)\end{cases} \qquad (32)$$

After integration on the volume of the beam element, with R^{ext} its external radius, the scalar product with the generalized coordinates becomes (33).

$$(E_i,E_j) = \frac{3}{2}\left(2\pi {R^{ext}}^2 L_0\right)\left[E1_iE1_j + {R^{ext}}^2\left(\frac{C2_iC2_j}{4}+\frac{C3_iC3_j}{4}\right)\right] \qquad (33)$$

After integration on the volume of the pipe element, with R^{int} and R^{ext} its internal and external radiuses, the scalar product with the generalized coordinates becomes (34).

$$(E_i, E_j) = \frac{3}{2}\left({R^{ext}}^2 - {R^{int}}^2\right) 2\pi L_0 \left[E1_i E1_j + \frac{\left({R^{ext}}^2 + {R^{int}}^2\right)}{2}\left(\frac{C2_i C2_j}{2} + \frac{C3_i C3_j}{2}\right)\right] \qquad (34)$$

The same reasoning applies to other generalized elements such as shell for example.

4.4 Modified POD for macroscopic displacement modes

In section 3.2.1, an arbitrary orthogonal basis of macroscopic displacement modes with 9 modes was chosen since there were 3 grids only. A FA has 10 grids and a top nozzle, leading to 33 elementary modes in 3D, if considering the bottom nozzle motionless. In order to use less modes, it is still possible to perform a POD on the displacements of the grids obtained by running the test plan. By carrying out such an exercise, the POD particularly highlights the axial thermal expansion modes, which are particularly visible because of the great length of the FA. However, these are less interesting to us than the lateral displacements of the grids. The authors therefore choose to weight the POD by a stiffness matrix K_{param} in (35) that favors the modes involving bending of the FA over the axial modes.

$$\begin{cases} \boldsymbol{U}^a\left(grid_g, t\right) \approx \sum_{j=1,J} \alpha_j(t)\, \boldsymbol{U}_j^a(grid_g) \\ (\boldsymbol{U}_k^a, \boldsymbol{U}_l^a) = \boldsymbol{U}_k^{at}.K_{param}.\boldsymbol{U}_l^a = \delta_{kl}, \forall(k,l)\epsilon[1,J]^2 \\ J = argmin_L\left(\frac{\sum_{k=1}^{L}\lambda_k}{\sum_{k=1}^{k\_max}\lambda_k} \geq 1-\rho\right) \end{cases} \qquad (35)$$

In practice, K_{param} is built as a stiffness matrix of a beam passing through the twelve nodes of the grid and nozzle, with a plain square section of 20x20cm², thus stiff enough in flexion to let the first ten modes present minor axial values. Fig. 10 pictures the 18 3D modes obtained with such a weighted POD, for a projection error ρ limited to 1%.

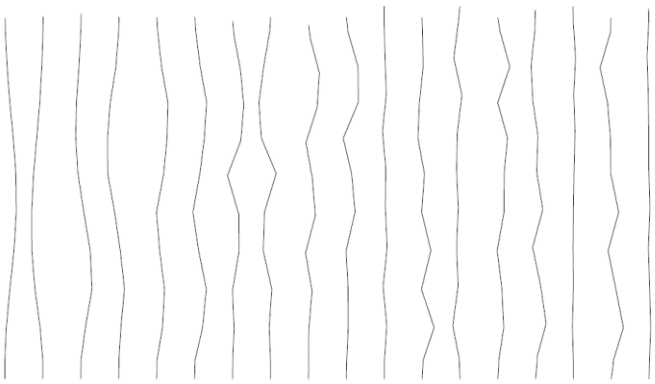

Fig. 10. 18 macroscopic displacement modes (3D), from a weighted POD on grid displacements with a truncation at 99%.

4.5 Inelastic modes

From the 88 simulations performed during the test plan, 176 creep strain snapshots were collected. A POD is applied using (34) to account for generalized strains in pipe elements. Fig. 11 displays the component CY of inelastic curvature for the 5 first tensor modes. This basis is truncated after 18 modes following the same criterion as for the macroscopic modes.

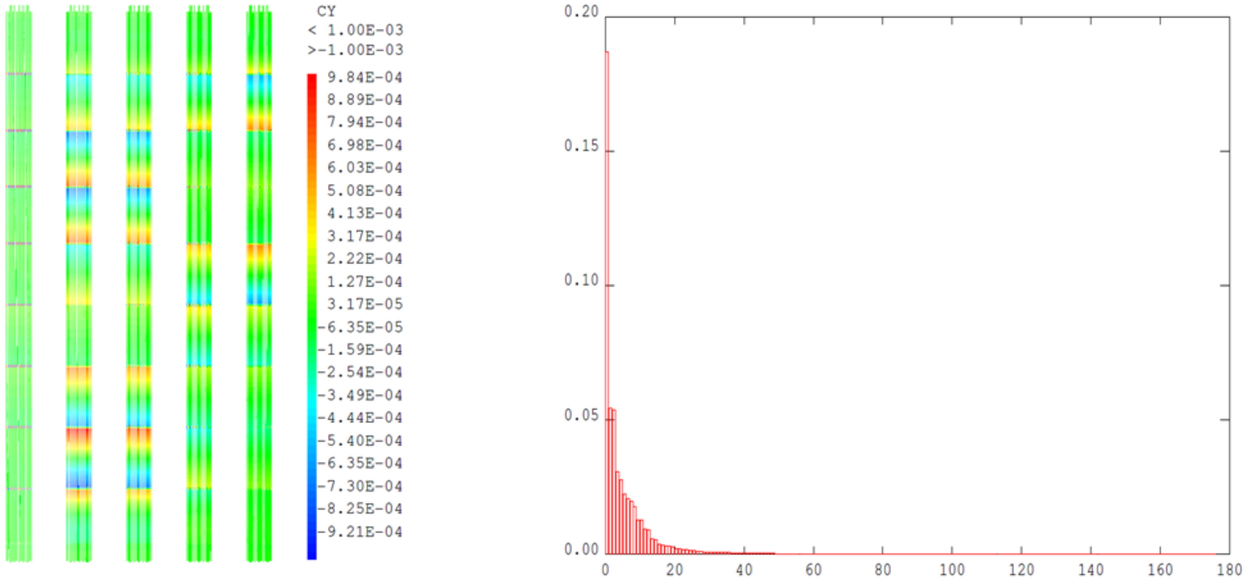

Fig. 11. Out of plane inelastic curvature CY of the 5 first inelastic tensor modes, POD eigenvalues of the 176 creep strain snapshots.

4.6 ROM verification on the points of the design of experiments

The 88 previous calculations that permitted to identify the modes and the operators were simulated using the ROM. For each calculation, the grid forces are projected onto the macroscopic displacement modes (16) and the modal creep characteristics (25,28) are determined from the considered neutron flux mapping (central or peripheral position). The grid displacement results are then compared in Fig. 12 for the first 7 calculation cases, which represent the LAT1 to LAT7 force loadings with a neutron flux corresponding to a central core position.

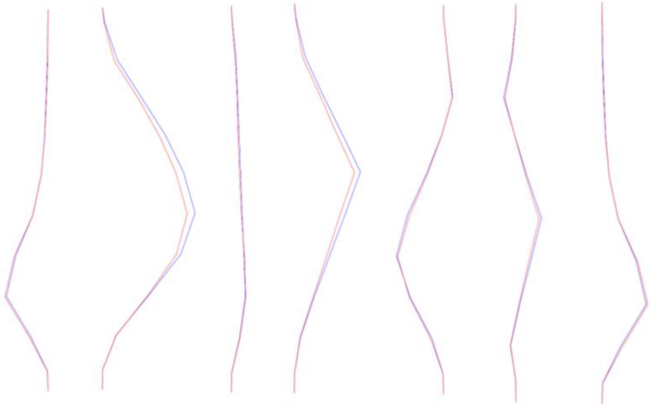

Fig. 12. Displacement comparison between the ROM results and the results of detailed FA model for the 7 load cases LAT1 to LAT7. ROM in red, reference in blue. Magnification x200.

Fig. 13. displays the same type of comparison for different cases but, this time, with forces applied in both horizontal directions at the same time. The precision is similar to the uncoupled loadings case.

Fig. 13. ROM grids displacements (red) compared to reference (blue) for coupled force loadings in horizontal directions X and Y. Left: forces LAT1/LAT2 – middle: LAT2/LAT3 – right: LAT2/LAT5. Magnification x200. Viewpoint chosen to maximize the visible displacement.

The inelastic deformation fields are also recombined and compared, in Fig. 14, to the creep fields of the reference calculation number 6. In this case, the ROM shows a good mapping and a slight deficit in axial creep intensity. Creep of the rods in curvature at the passage of each grid is larger and well correlated.

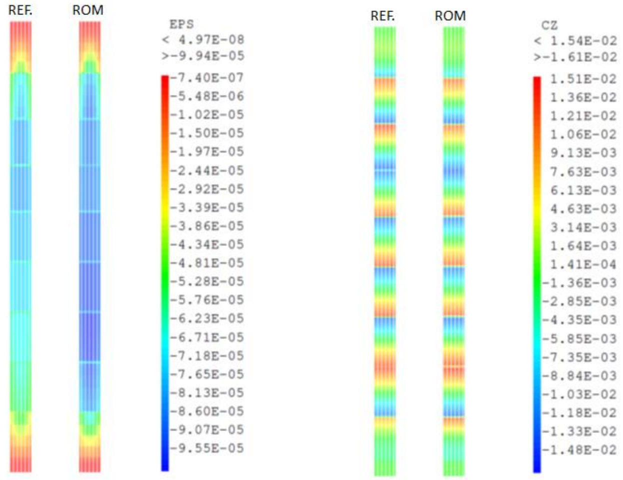

Fig. 14. Creep comparison for loading LAT6. Left: axial creep strain. Right: creep curvature in the rods (rad/m).

In order to give a more statistical view of the error committed with the FA ROM, one can define an indicator (36) for the creep flow error on one given trajectory. This indicator relies on the local dissipation difference between the reference model and the recombined fields of the ROM, integrated over space and time

$$e_{flow} = \left(\int_0^T \iiint_\Omega \left| \sigma_{ref} : \dot{\varepsilon}_{ref}^{vp} - \left(\sum_{i=1}^{I} \alpha_i^{in} \boldsymbol{\sigma}_i^{in\_asso} + \sum_{j=1}^{J} \alpha_j^{in} \boldsymbol{\sigma}_j^{a\_asso} \right) : \left(\sum_{i=1}^{I} \dot{\alpha}_i^{in} \, \varepsilon_i^{in} \right) \right| d\Omega dt \right)^{1/2} \qquad (36)$$

The global relative flow error re_{flow}^{val}, evaluated for all the 88 realizations of the experimental design, takes the form (37) and establishes to 14%.

$$re_{flow}^{val} = \frac{\sum_{s=1}^{Nt} \left(e_{flow}(s) \right)^2}{\sum_{s=1}^{Nt} \left(\int_0^T \iiint_\Omega \sigma(s) : \dot{\varepsilon}^{vp}(s) d\Omega dt \right)} \qquad (37)$$

Concerning the calculation time, table 10 shows a speed-up of around 50 for this FA creep simulation, comparable to the speed-up of 110 realized with the lighter prototypic FA model, see table 4 in 3.3. The reason for this lower speed-up is that the FA reference model is already highly optimized and uses exclusively generalized finite elements, such as pipes and shells. Obviously, the same geometry represented by a classical mesh of linear or quadratic brick elements would have displayed a much better time ratio.

Table 10: typical computing time (1 processor) for a FA creep calculation.

Reference model (Cast3M)	ROM: 18 displacement modes / 18 creep modes
866s	16s

4.7 Validation outside the characterization points

The objective of this section is to verify that the results of the ROM remain valid outside the points used for its construction. For this, a completely new test case is defined and simulated with both the detailed and the reduced models.

The test conditions consider a FA in a near peripheral core position, subjected to new lateral forces summarized in table 11. These forces are not collinear with any of the loadings used to identify the ROM. The axial compression value, which was 5000N in all the previous calculations, is now increased to 6000N.

Table 11: new lateral loading definition for interpolation test case 1, the neutron flux remains unchanged.

Grid	1	2	3	4	5	6	7	8	9	10
Force Fx (N)	40	20	0	-10	-60	-70	-35	0	13	20
Force Fy (N)	0	-28	-56	-32	0	12	44	42	23	0

Concerning the neutron flux field, lateral gradients of neutron flux are added, respectively of 30% in the X direction and 20% in the Y direction. These lateral gradients can be seen as an interpolation of the 3 neutron flux maps previously used. In addition, a small extrapolation of the parameter space is also operated, resulting in an axial power offset, see Fig. 15, whereas no sensitivity was performed on this axis in the initial realizations. In fact, the modal creep characteristics are affected by this new neutron flux field through Eq. (25,28) , which precisely capture its influence on every mode individually.

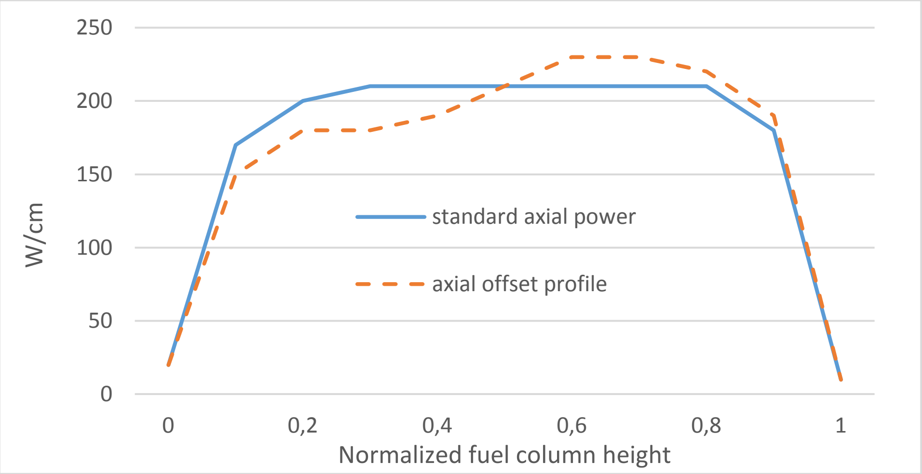

Fig. 15. Axial rod power profiles, standard case in blue, axial offset in orange as used in test case 2.

The results of the ROM are compared to those of the detailed model in Fig. 16, for displacements, axial creep and curvature creep. The final deformed shape, recombined from the ROM solution, is close to the reference model and so are the axial and curvature creep fields. However, when looking precisely at the creep curvature comparison at the right in Fig. 16, one should note that the ROM slightly underestimates the intensity at the bottom of the FA and slightly overestimates it at the top. This is due to the basis of creep modes that was built on snapshots obtained with symmetric axial flux only (see Fig. 15).

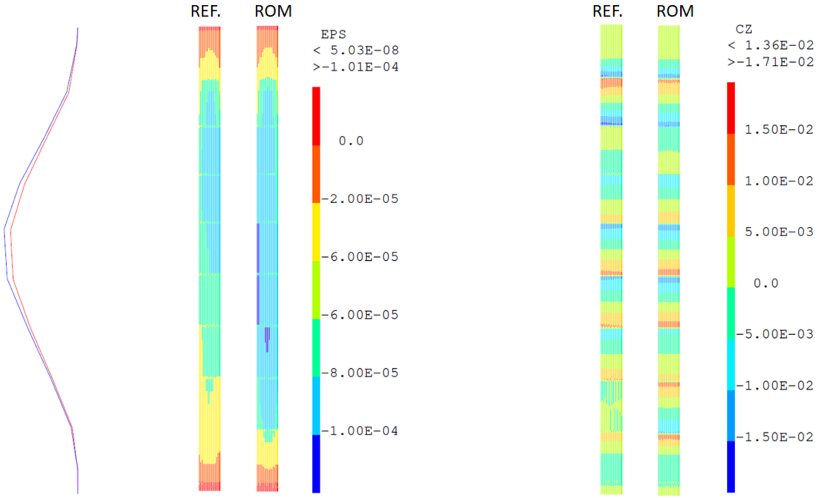

Fig. 16. Test case with light extrapolation, on the left, comparison of the deformed shape of ROM, in red, with reference model, in blue (magnitude 200). In the middle, comparison of axial creep strain of the rods. On the right, comparison of creep curvature of the rods (rad/m).

These results confirm the expected ROM ability to interpolate in the parameter space and, to some extent, extrapolate. Of course, any extrapolation should be done with caution since a completely different neutron flux could possibly generate very different creep modes.

5. Conclusions and perspectives

The authors have proposed a new method for model reduction in structural mechanics with nonlinear behavior laws. This method results from an adaptation of the NTFA homogenization method to complex slender structures considered as a unique RVE. Compared to the classical simplified FE models of FA, it gives access to local quantities at any point in the structure for additional post-processing. Above all, many simplifying assumptions are avoided here, in particular on the rigidity of the grids and on the neutron flux gradients.

It has been successfully applied to a detailed model of a PWR FA in a quasi-static framework. Necessary adaptations are developed to match with the pipes and shell elements used in the reference FA model. A second improvement was introduced to account for the heterogeneous creep characteristics by weighting the inelastic modes individually. This allows taking into account the effect of neutron flux mapping on creep, including at an intra-assembly scale, which is particularly useful for assemblies at the core periphery.

The accuracy obtained during the tests is very satisfactory, including for cases of force interpolation and reasonable axial flow extrapolation, thanks to the modal creep characteristic definition tailored to the heterogeneous material characteristics.

The speed-up obtained allows the prospect of fast simulations. This is due to the definition of global modes directly on the structure (only one RVE per FA) and to the fact that only one integration of the nonlinear behavior is performed for a whole phase of the structure.

In accordance with the final objective, the developments carried out and to come at the scale of a FA will make it possible, in the near future, to set up calculations of complete core, coupling hydraulic with mechanics. The reduced model of a FA will be repeated as many times as necessary, allowing for a good compromise between accuracy and computing cost at the core scale.

Future work will introduce the consideration of heterogeneous thermal expansion. For this, it is only necessary to define a new transformation following the thermal expansion rules. Like (Roussette et al., 2009) did to treat the isotropic fuel swelling with the NTFA approach, it appeals for compressible modes, obtained by POD, and the resulting associated stress fields will have a non-zero projection on the inelastic creep modes.

Finally, the authors are currently developing a reduction of the contact-friction problem inside the fuel assembly, based on (Balajewicz et al., 2016). It is formulated in coherence with the creep reduction method that was just presented and shows promising results. The combination of these two methods will soon allow representing with a good spatial definition the sliding between rods and grids as well as the long term creep strains.

Although not intended for this purpose, this type of lightweight thermomechanical model could also potentially provide the basis regarding non-linear dynamics. The main difficulty would then lie in the accurate prediction of the fluid-structure interaction between the different assemblies within the PWR core, which remains a very open subject (Divaret et al., 2014; Faucher et al., 2021; Ricciardi, 2022).

References

Ammar, A., Chinesta, F., 2008. Circumventing Curse of Dimensionality in the Solution of Highly Multidimensional Models Encountered in Quantum Mechanics Using Meshfree Finite Sums Decomposition, in: Meshfree Methods for Partial Differential Equations IV. Springer, Berlin, Heidelberg, pp. 1–17.

Andersson, T., Almberger, J., Bjoernkvist, L., 2005. A decade of assembly bow management at Ringhals (No. 1011–4289). International Atomic Energy Agency (IAEA).

Balajewicz, M., Amsallem, D., Farhat, C., 2016. Projection-based model reduction for contact problems. Int. J. Numer. Methods Eng. 106, 644–663. https://doi.org/10.1002/nme.5135

Barrault, M., Maday, Y., Nguyen, N.C., Patera, A.T., 2004. An “empirical interpolation” method: application to efficient reduced-basis discretization of partial differential equations. Comptes Rendus Math. 339, 667–672. https://doi.org/10.1016/j.crma.2004.08.006

CEA, 2020. Cast3m finite element software [WWW Document]. Cast3M Code Aux Éléments Finis CEA. URL http://www-cast3m.cea.fr/

Chaboche, J.L., Kruch, S., Maire, J.F., Pottier, T., 2001. Towards a micromechanics based inelastic and damage modeling of composites. Int. J. Plast. 17, 411–439. https://doi.org/10.1016/S0749-6419(00)00056-5

De Lambert, S., Campioni, G., Faucher, V., Leturcq, B., Cardolaccia, J., 2019. Modeling the consequences of fuel assembly bowing on PWR core neutronics using a Monte-Carlo code. Ann. Nucl. Energy 134, 330–341. https://doi.org/10.1016/j.anucene.2019.06.017

De Lambert, S., Cardolaccia, J., Faucher, V., Thomine, O., Leturcq, B., Campioni, G., 2021. Semi-analytical modeling of the flow redistribution upstream from the mixing grids in a context of nuclear fuel assembly bow. Nucl. Eng. Des. 371, 110940. https://doi.org/10.1016/j.nucengdes.2020.110940

Divaret, L., Moussou, P., Berland, J., Berro, H., Cadot, O., Doaré, O., 2014. Forces Exerted on a Cylinder in Near-Axial Flow. J. Press. Vessel Technol. 136. https://doi.org/10.1115/1.4026567

Dumon, A., Allery, C., Ammar, A., 2011. Proper general decomposition (PGD) for the resolution of Navier–Stokes equations. J. Comput. Phys. 230, 1387–1407. https://doi.org/10.1016/j.jcp.2010.11.010

Dvorak, G.J., 1992. Transformation field analysis of inelastic composite materials. Proc. R. Soc. Lond. Ser. Math. Phys. Sci. 437, 311–327. https://doi.org/10.1098/rspa.1992.0063

Elbanhawy, O., Hassan, M., Mohany, A., 2021. Modelling of fully-flexible fuel bundles. Nucl. Eng. Des. 378, 111014. https://doi.org/10.1016/j.nucengdes.2020.111014

Faucher, V., Ricciardi, G., Boccaccio, R., Cruz, K., Lohez, T., Clément, S.A., 2021. Numerical implementation and validation of a porous approach for fluid–structure interaction applied to pressurized water reactors fuel assemblies under axial water flow and dynamic excitation. Int. J. Numer. Methods Eng. 122, 2417–2445. https://doi.org/10.1002/nme.6626

Fauque, J., Ramière, I., Ryckelynck, D., 2018. Hybrid hyper-reduced modeling for contact mechanics problems. Int. J. Numer. Methods Eng. 115, 117–139. https://doi.org/10.1002/nme.5798

Fernandes, R., 2010. Modélisation de la déformation d’assemblages combustibles d’une centrale REP.

Fidleris, V., 1988. The irradiation creep and growth phenomena. J. Nucl. Mater. 159, 22–42. https://doi.org/10.1016/0022-3115(88)90083-9

Fish, J., Shek, K., 1999. Finite deformation plasticity for composite structures: Computational models and adaptive strategies. Comput. Methods Appl. Mech. Eng. 172, 145–174. https://doi.org/10.1016/S0045-7825(98)00228-X

Fournier, Y., Vurpillot, C., Béchaud, C., 2007. Evaluation of fluid flow in the lower core of a PWR with Code_Saturne. Nucl. Eng. Des. 237, 1729–1744. https://doi.org/10.1016/j.nucengdes.2007.02.025

Gabrielsson, P., Schrire, D., Suvantseg, E., Malmerg, M., 2018. Investigation of the development of fuel assembly bow Ringhals 3 and 4. Presented at the TOPFUEL2018 reactor fuel performance, European Nuclear Society, Prague, Czech Republic.

Geelhood, K.J., Luscher, W.G., Beyer, C.E., 2011. FRAPCON-3.4 : A Computer Code for the calculation of Steady-State, Thermal-Mechanical Behavior of Oxide Fuel Rods for High Burnup (No. NUREG/CR-7022, Vol. 1). USNRC, Richland, WA 99352.

Gharbi, N., 2015. Contribution à la compréhension de la déformation sous irradiation des alliages de zirconium à forte dose (PhD Thesis). Université de La Rochelle.

Gilbon, D., Soniak, A., Doriot, S., Mardon, J.-P., 2000. Irradiation Creep and Growth Behavior, and Microstructural Evolution of Advanced Zr-Base Alloys, in: Sabol, G., Moan, G. (Eds.), Zirconium in the Nuclear Industry: Twelfth International Symposium. ASTM International, pp. 51-51–23.

Hammoud, M., Béringhier, M., Grandidier, J.-C., 2011. Application de la PGD à un problème viscoélastique avec un grand nombre de variables internes et un large spectre de temps de relaxation, in: 10e Colloque National En Calcul Des Structures. Giens, France.

Hassan, M.A., Rogers, R.J., 2005. Friction modelling of preloaded tube contact dynamics. Nucl. Eng. Des. 235, 2349–2357. https://doi.org/10.1016/j.nucengdes.2005.05.004

Hernández, J.A., Caicedo, M.A., Ferrer, A., 2017. Dimensional hyper-reduction of nonlinear finite element models via empirical cubature. Comput. Methods Appl. Mech. Eng. 313, 687–722. https://doi.org/10.1016/j.cma.2016.10.022

Horváth, Á., Dressel, B., 2013. On numerical simulation of fuel assembly bow in pressurized water reactors. Nucl. Eng. Des. 265, 814–825. https://doi.org/10.1016/j.nucengdes.2013.09.031

IAEA, 2010. Review of fuel failures in water cooled reactors, fuel structural damage and other fuel assembly issues, Nuclear Energy Series. International Atomic Energy Agency, Vienna. ISBN 978-92-0-102610-1.

Jeon, S.Y., 2009. An Investigation on the Fuel Assembly Structural Performance for the PLUS7TM Fuel Design. Presented at the 20th International Conference on Structural Mechanics in Reactor Technology, Espoo, Finland, p. Division 6, Paper 1824.

Karhunen, K., 1946. über lineare methoden in der wahrscheinli. Ann. Acad. Sci. Fenn., Mathematica-Physica, 37 Series A1, 1–79.

Kecek, A., Tuček, K., Van Uffelen, P., Holmström, Stefan, 2016. Development of M5 cladding material correlations in the TRANSURANUS code: revision 1., JRC Technical Reports. ed. Joint Research Centre. ISBN 978-92-79-64655-3.

Ladeveze, P., 1985. Sur une famille d'algorithmes en mécanique des structures. (An algorithm family in structural mechanics). Comptes Rendus Académie Sci.

Lamorte, N., Méry de Montigny, E., Goreaud, N., Chazot, B., Marx, V., 2021. Advanced predictive tool for fuel assembly bow design performance evaluations. Presented at the TOP FUEL 2021, Santander, Spain.

Largenton, R., Michel, J.-C., Suquet, P., 2013. Optimisation de l'analyse en champs de transformation non uniformes pour le comportement du combustible MOX en service., in: 11ème Colloque National En Calcul Des Structures (CSMA 2013). Giens, France, p. 8.

Lascar C., 2015. Advanced predictive tool for fuel ssembly bow based on a 3d coupled fsi approach. Presented at the TOPFUEL 2015, European Nuclear Society, Zurich, Switzerland, pp. 323–331.

Lumley, J.L., 1967. The structure of inhomogeneous turbulent flows. Atmospheric Turbul. Radio Wave Propag. 166–178.

Metoui, S., Pruliere, E., Ammar, A., Dau, F., Iordanoff, I., 2014. The proper generalized decomposition for the simulation of delamination using cohesive zone model: THE PGD FOR SIMULATIONS USING COHESIVE ZONE MODEL. Int. J. Numer. Methods Eng. 99, 1000–1022. https://doi.org/10.1002/nme.4732

Michel, J.C., Suquet, P., 2016. A model-reduction approach to the micromechanical analysis of polycrystalline materials. Comput. Mech. 57, 483–508. https://doi.org/10.1007/s00466-015-1248-9

Michel, J.C., Suquet, P., 2004. Computational analysis of nonlinear composite structures using the nonuniform transformation field analysis. Comput. Methods Appl. Mech. Eng. 193, 5477–5502. https://doi.org/10.1016/j.cma.2003.12.071

Michel, J.C., Suquet, P., 2003. Nonuniform transformation field analysis. Int. J. Solids Struct. 40, 6937–6955. https://doi.org/10.1016/S0020-7683(03)00346-9

Pramuditya, S., 2009. Standard PWR nuclear fuel assembly (17×17) technical specification. Hey Whats Going On. URL https://syeilendrapramuditya.wordpress.com/2009/04/14/standard-pwr-nuclear-fuel-assembly-17x17-technical-specification/ (accessed 5.4.22).

Ricciardi, G., 2022. Analytical model of added mass, damping and stiffness of a fuel assembly induced by axial flow. Nucl. Eng. Des. 389, 111670. https://doi.org/10.1016/j.nucengdes.2022.111670

Ricciardi, G., 2017. Dynamical Nonlinear Modelling Of A Pressurised Water Reactor Fuel Assembly Subjected To An Axial Flow. Procedia Eng. 199, 1314–1319. https://doi.org/10.1016/j.proeng.2017.09.309

Rice, J.R., 1970. On the Structure of Stress-Strain Relations for Time-Dependent Plastic Deformation in Metals. J. Appl. Mech. 37, 728–737. https://doi.org/10.1115/1.3408603

Richardson, L.F., Glazebrook, R.T., 1911. IX. The approximate arithmetical solution by finite differences of physical problems involving differential equations, with an application to the stresses in a masonry dam. Philos. Trans. R. Soc. Lond. Ser. Contain. Pap. Math. Phys. Character 210, 307–357. https://doi.org/10.1098/rsta.1911.0009

Roussette, S., Michel, J.C., Suquet, P., 2009. Nonuniform transformation field analysis of elastic–viscoplastic composites. Compos. Sci. Technol. 69, 22–27. https://doi.org/10.1016/j.compscitech.2007.10.032

Ryckelynck, D., 2009. Hyper-reduction of mechanical models involving internal variables. Int. J. Numer. Methods Eng. 77, 75–89. https://doi.org/10.1002/nme.2406

Saeed, A., Bakr, M.A., Saqib, A.U., 2016. Estimation of Axial and radial in-core power peaking in PWR plant using artificial neural network technique. IEEE, pp. 1–6. https://doi.org/10.1109/ICET.2016.7813216

Scholz, R., Matera, R., 2000. Irradiation creep induced stress relaxation of Inconel 718. Fusion Eng. Des. 51–52, 165–170. https://doi.org/10.1016/S0920-3796(00)00313-6

Sheng, D.-Y., Seidl, M., 2015. Towards the development of a full-scale transient cfd model to simulate the static and dynamic in-core mass flux distribution in a classical german PWR. Presented at the NURETH-16th International Topical Meeting on Nuclear Reactor Thermalhydraulics, Chicago, IL.

Sirovich, L., 1987. Turbulence and the dynamics of coherent structures. I. Coherent structures. Q. Appl. Math. 45, 561–571. https://doi.org/10.1090/qam/910462

Wanninger, A., 2018. Mechanical analysis of the bow deformations of the fuel assemblies in a pressurized water reactor core. Technische universitat München, München.

Wanninger, A., Seidl, M., Macian, R., 2016. Screening sensitivity analysis of a PWR fuel assembly FEM structural model. Presented at the Top Fuel 2016, Advanced Nuclear Sciences, Boise, ID.

Wanninger, A., Seidl, M., Macián-Juan, R., 2018. Mechanical analysis of the bow deformation of a row of fuel assemblies in a PWR core. Nucl. Eng. Technol. 50, 297–305. https://doi.org/10.1016/j.net.2017.12.009